

SPARTA: Spatial Acceleration for Efficient and Scalable Horizontal Diffusion Weather Stencil Computation

Gagandeep Singh^{a,b} Alireza Khodamoradi^a Kristof Denolf^a Jack Lo^a
Juan Gómez-Luna^b Joseph Melber^a Andra Bisca^a
Henk Corporaal^c Onur Mutlu^b
^aAMD Research ^bETH Zürich ^cEindhoven University of Technology

ABSTRACT

Fast and accurate climate simulations and weather predictions are critical for understanding and preparing for the impact of climate change. Real-world climate and weather simulations involve the use of complex compound stencil kernels, which are composed of a combination of different stencils. Horizontal diffusion is one such important compound stencil found in many climate and weather prediction models. Its computation involves a large amount of data access and manipulation that leads to two main issues on current computing systems. First, such compound stencils have high memory bandwidth demands as they require large amounts of data access. Second, compound stencils have complex data access patterns and poor data locality, as the memory access pattern is typically irregular with low arithmetic intensity. As a result, state-of-the-art CPU and GPU implementations suffer from limited performance and high energy consumption. Recent works propose using FPGAs as an alternative to traditional CPU and GPU-based systems to accelerate weather stencil kernels. However, we observe that stencil computation cannot leverage the bit-level flexibility available on an FPGA because of its complex memory access patterns, leading to high hardware resource utilization and low peak performance.

We introduce SPARTA, a novel spatial accelerator for horizontal diffusion weather stencil computation. We exploit the two-dimensional spatial architecture to efficiently accelerate the horizontal diffusion stencil by designing the first scaled-out spatial accelerator using the MLIR (Multi-Level Intermediate Representation) compiler framework. We evaluate SPARTA on a real cutting-edge AMD-Xilinx Versal AI Engine (AIE) spatial architecture. Our real-system evaluation results demonstrate that SPARTA outperforms state-of-the-art CPU, GPU, and FPGA implementations by 17.1×, 1.2×, and 2.1×, respectively. Compared to the most energy-efficient design on an HBM-based FPGA, SPARTA provides 2.43× higher energy efficiency. Our results reveal that balancing workload across the available processing resources is crucial in achieving high performance on spatial architectures. We also implement and evaluate five elementary stencils that are commonly used as benchmarks for

Permission to make digital or hard copies of all or part of this work for personal or classroom use is granted without fee provided that copies are not made or distributed for profit or commercial advantage and that copies bear this notice and the full citation on the first page. Copyrights for components of this work owned by others than the author(s) must be honored. Abstracting with credit is permitted. To copy otherwise, or republish, to post on servers or to redistribute to lists, requires prior specific permission and/or a fee. Request permissions from permissions@acm.org.

ICS '23, June 21–23, 2023, Orlando, FL, USA

© 2023 Copyright held by the owner/author(s). Publication rights licensed to ACM.

ACM ISBN 979-8-4007-0056-9/23/06...\$15.00

<https://doi.org/10.1145/3577193.3593719>

stencil computation research. We freely open-source all our implementations to aid future research in stencil computation and spatial computing systems at <https://github.com/CMU-SAFARI/SPARTA>.

CCS CONCEPTS

• **Hardware** → **Hardware-software codesign; Emerging architectures**; • **Computer systems organization** → **Parallel architectures; Data flow architectures**.

KEYWORDS

spatial computing systems, dataflow architectures, high-performance computing, hybrid systems, weather prediction, stencil computation, memory access patterns, climate modeling

ACM Reference Format:

Gagandeep Singh, Alireza Khodamoradi, Kristof Denolf, Jack Lo, Juan Gómez-Luna, Joseph Melber, Andra Bisca, Henk Corporaal, Onur Mutlu. SPARTA: Spatial Acceleration for Efficient and Scalable Horizontal Diffusion Weather Stencil Computation. In *2023 International Conference on Supercomputing (ICS '23)*, June 21–23, 2023, Orlando, FL, USA. ACM, New York, NY, USA, 14 pages. <https://doi.org/10.1145/3577193.3593719>

1 INTRODUCTION

Climate simulations and weather predictions are essential for understanding and preparing for the impacts of climate change. The ability to make fast and accurate predictions is one of the biggest challenges meteorologists face to ensure effective and timely responses [1–11]. Researchers use mathematical models to simulate and analyze the behavior of the Earth’s ecosystem. These models are based on fundamental physical and chemical principles and are continuously refined to improve their accuracy [12, 13]. The Consortium for Small-Scale Modeling (COSMO) [14] is one such model that is extensively used in weather forecasting, numerical weather prediction, and climate studies.

The main computational pipeline of COSMO, called the *dycore* or the dynamical core, consists of compound stencil kernels that operate on a three-dimensional grid [13, 15]. Horizontal diffusion (*hdiff*) is a fundamental kernel found in the dynamical core of COSMO and other regional and global climate and weather prediction models [13, 15, 16], including the European Centre for Medium-Range Weather Forecasts (ECMWF) model [17] and the Global Forecast System (GFS) model [18]. It is also used in climate models, such as the Community Earth System Model (CESM) [19] and the Model for Interdisciplinary Research on Climate (MIROC) [20]. The main use of horizontal diffusion is to help reduce the impact of small-scale errors in the model, such as those caused by the limited resolution of the model or by the effects of small-scale atmospheric processes

that are not well represented by the model [21]. By applying horizontal diffusion, the model can better represent the large-scale flow of the atmosphere and produce more accurate forecasts [22].

Recent works propose the use of FPGAs [16, 23–29] as an alternative to traditional CPU and GPU-based systems in accelerating such weather stencil-based workloads due to FPGA’s customizability to computation patterns. However, we observe three main issues. First, compound stencil computation cannot leverage the bit-level flexibility available on an FPGA because of its complex memory access patterns, leading to high hardware resource utilization. Second, the difficulty of designing and implementing efficient algorithms on FPGAs has been an impediment against broad, high-volume adoption. Third, stencils in weather and climate simulations, such as horizontal diffusion, can be parameterized using different coefficients, which would entail designing a different hardware accelerator for each parameterization scheme.

Figure 1 shows roofline plots [30] for an IBM server-grade POWER9 CPU-based [31] and NVIDIA V100 GPU [32] from the state-of-the-art `hdiff` CPU- [24] and GPU-based [16] implementations, respectively. It also shows the roofline for an HBM-based AD9H7 FPGA [33] used in the state-of-the-art `hdiff` implementation work [24]. We make the following two major observations. First, `hdiff` cannot achieve peak performance on a given architecture and often results in only 6.1%–13.5% of the peak performance (i.e., the percentage of achieved peak roofline performance) on current multi-core, GPU, and FPGA-based architectures. Its performance is dominated by memory-bound operations with unique irregular memory access patterns and low arithmetic intensity that often results in poor performance on current systems. Second, `hdiff` is not able to leverage the bit-level programmability of an FPGA because of complex memory access patterns leading to high resource usage as it spends a large fraction of time on irregular memory operations.

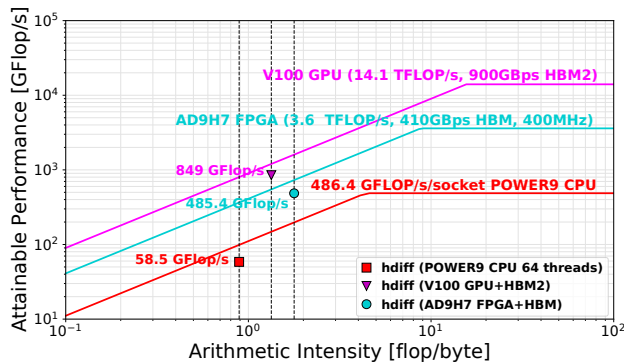


Figure 1: Roofline [30] for POWER9 (1-socket) showing horizontal diffusion (`hdiff`) kernel for 64-thread implementation. The plot also shows the rooflines of HBM-based NVIDIA V100 GPU [32] and AD9H7 FPGA [33] with peak DRAM bandwidth.

Recently, several spatial architectures, such as AMD-Xilinx Versal AI Engine [34], Groq Tensor Streaming Processor [35], Intel’s Configurable Spatial Accelerator [36], and Cerebras Deep Neural Network Accelerator [37], have been proposed to accelerate machine learning-based workloads [38, 39]. These architectures

consist of an array of small processing cores that are interconnected through a highly configurable network. The primary focus of these spatial architectures has been to provide a more efficient and effective way to accelerate machine learning workloads. However, we observe that spatial architectures can overcome the limitations of accelerating stencil computations on traditional architectures due to three reasons. First, unlike FPGAs, which offer bit-level flexibility, spatial architectures provide coarse-grained flexibility that allows for tailoring of the dataflow to optimize data movement. Second, the two-dimensional layout of spatial architectures maps well to processing multi-dimensional grids, making them well-suited for stencil computation. Third, the dataflow design of spatial architectures provides an intuitive way to take advantage of both spatial and temporal locality in iterative stencil processing by pipelining different timesteps. Therefore, spatial architectures have the potential to enable highly efficient processing of weather stencil computation, leading to improved performance and scalability.

Our goal is to mitigate the performance bottleneck of memory-bound weather stencil computations by taking advantage of the characteristics of spatial computing systems.

To this end, we introduce SPARTA, a novel spatial accelerator for horizontal diffusion stencil computation. We evaluate SPARTA on the real cutting-edge AMD-Xilinx Versal [34] spatial architecture. This architecture offers coarse-grained acceleration through the implementation of Vector VLIW (Very Long Instruction Word) [40] processing cores, known as AI Engines (AIEs). We tailor the horizontal diffusion algorithm to fit well into the spatial architecture datapath that optimizes data movement. Our evaluation results show that SPARTA achieves 17.1 \times , 1.2 \times , and 2.1 \times higher performance compared to the state-of-the-art CPU, GPU, and FPGA implementations of horizontal diffusion, respectively. Compared to the most energy-efficient design on an HBM-based FPGA, SPARTA provides 2.43 \times higher energy efficiency. Our results indicate that spatial architectures can mitigate current technological limitations for weather stencil computation.

This work makes the following major contributions:

- We perform a detailed analysis to show that the fundamental weather prediction kernel is constrained by memory bandwidth on state-of-the-art CPU, GPU, and FPGA-based systems.
- We introduce SPARTA, the first spatial accelerator for horizontal diffusion stencil from a real-world weather model. This work is the first to propose and evaluate a real spatial architecture specifically for weather stencil computation, as opposed to commonly used machine learning-based workloads.
- We provide the first scaled-out spatial accelerator design using the multi-level intermediate representation (MLIR) framework. We analyze: 1) floating and fixed pipeline datapaths, and 2) multi-core design using different interconnects on a real cutting-edge spatial architecture, the AMD-Xilinx Versal AI Engine.
- We conduct an in-depth evaluation of SPARTA on a real system showing that it outperforms state-of-the-art CPU, GPU, and FPGA-based implementations in terms of execution time. We open-source our implementations, including five elementary stencils that are commonly used as benchmarks for stencil computation research, to aid further research in accelerating stencil computation on spatial architectures at <https://github.com/CMU-SAFARI/SPARTA>.

2 BACKGROUND

2.1 Horizontal Diffusion Weather Stencil

A stencil operation sweeps over an input grid, updating values based using a fixed computation pattern. High-order stencils are applied to multidimensional grids that have sparse and irregular memory access patterns, limiting the achievable performance. In addition, stencils have limited cache data reuse which further enhances memory access pressure. Unlike stencils found in the literature [16, 27, 41–45], real-world compound stencils [13, 15] consist of a collection of stencils that perform a sequence of element-wise computations with complex interdependencies. Horizontal diffusion (`hdiff`) represents one such fundamental compound stencil found in the dynamical core of the COSMO weather model [13, 15].

Horizontal diffusion is a process used in numerical weather prediction models to help smooth out small-scale variations in the atmosphere and reduce the impact of numerical errors. It is a mathematical technique used to represent the turbulent mixing of the atmosphere, which occurs due to the winds and temperature gradients in the atmosphere. Horizontal diffusion is used in a variety of other local and global weather prediction models [13, 15–20]. We can write the `hdiff` equations as follows [13]:

$$L_{r,c,d}^n = 4\psi_{r,c,d}^n - \psi_{r+1,c,d}^n - \psi_{r-1,c,d}^n - \psi_{r,c+1,d}^n - \psi_{r,c-1,d}^n \quad (1)$$

$$F_{r+\frac{1}{2},c,d}^n = \begin{cases} L_{r+1,c,d}^n - L_{r,c,d}^n & \text{if } (L_{r+1,c,d}^n - L_{r,c,d}^n) \\ & (\psi_{r+1,c,d}^n - \psi_{r,c,d}^n) \leq 0 \\ 0 & \text{otherwise} \end{cases} \quad (2)$$

$$G_{r,c+\frac{1}{2},d}^n = \begin{cases} L_{r,c+1,d}^n - L_{r,c,d}^n & \text{if } (L_{r,c+1,d}^n - L_{r,c,d}^n) \\ & (\psi_{r,c+1,d}^n - \psi_{r,c,d}^n) \leq 0 \\ 0 & \text{otherwise} \end{cases} \quad (3)$$

$$\Psi_{r,c,d}^{n+1} = \psi_{r,c,d}^n - C_{r,c,d}^n (F_{r+\frac{1}{2},c,d}^n - F_{r-\frac{1}{2},c,d}^n + G_{r,c+\frac{1}{2},d}^n - G_{r,c-\frac{1}{2},d}^n) \quad (4)$$

ψ represents the input data field at timestep n . $L_{r,c,d}^n$ is the discretized Laplacian (or Laplace operator) in Equation 1 over row, column, and depth dimensions of an input grid. While $F_{r+\frac{1}{2},c,d}^n$ and $G_{r,c+\frac{1}{2},d}^n$ represent limited fluxes along horizontal axes in Equations 2 and 3, respectively. In Equation 4, $\Psi_{r,c,d}^{n+1}$ represents the diffused output using a diffusion coefficient, $C_{r,c,d}^n$. The horizontal diffusion coefficients are used to represent the strength of the mixing, and are typically based on the physical properties of the atmosphere, such as wind speed and temperature. The coefficients are usually chosen based on the model resolution, and can be adjusted to account for the effects of small-scale atmospheric processes.

`hdiff` iterates over a 3D grid performing *Laplacian* and *flux*, as depicted in Figure 2, to calculate different grid points. Each color represents a different stencil pattern that is a part of the `hdiff` computation. A *Laplacian* stencil accesses the input grid at five memory offsets in horizontal dimensions. The output of the *Laplacian* stencil is used to calculate the *flux* stencil. The *flux* stencil also requires access to the input data for computation (indicated by a dashed arrow in Figure 2). `hdiff` has data dependencies in the horizontal neighborhood, therefore, we can parallelize `hdiff` in the vertical dimension.

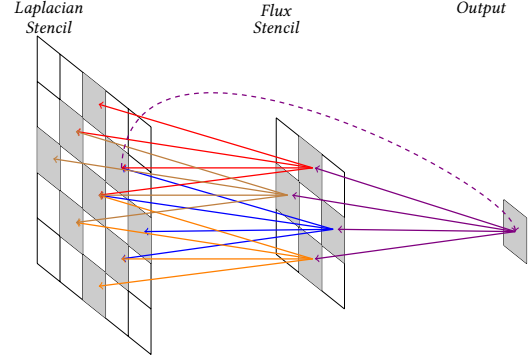


Figure 2: `hdiff` kernel composition using Laplacian and flux stencils in a two-dimensional plane [23]. Each color represents a different stencil pattern that is a part of the `hdiff` computation. The dashed arrow represents the dependency of the flux stencil on the input data.

Algorithm 1 shows a pseudo-code for the fourth-order `hdiff` (i.e., the order of the highest derivative, also known as differential coefficient, is four for `hdiff`).

Algorithm 1: Pseudo-code for horizontal diffusion (`hdiff`) kernel used by the COSMO [14] weather prediction model.

```

1 Func hdiff(float* src, float* dst)
2   for d ← 1 to depth do
3     for c ← 2 to column - 2 do
4       for r ← 2 to row - 2 do
5         // Laplacian calculation
6         lapCR = laplaceCalculate(c, r)
7         // row-laplacian
8         lapCRm = laplaceCalculate(c, r - 1)
9         lapCRp = laplaceCalculate(c, r + 1)
10        // column-laplacian
11        lapCMR = laplaceCalculate(c - 1, r)
12        lapCMR = laplaceCalculate(c + 1, r)
13        // column-flux calculation
14        fluxC = lapCMR - lapCR
15        fluxCM = lapCR - lapCMR
16        // row-flux calculation
17        fluxR = lapCRp - lapCR
18        fluxRm = lapCR - lapCRp
19        // output calculation
20        dest[d][c][r] = src[d][c][r] - c1 * (fluxCR -
21        fluxCMR) + (fluxCR - fluxCMR)
22      end
23    end
24  end

```

Figure 3 shows the memory layout for the horizontal diffusion kernel. `hdiff` computation typically involves a large amount of data access and manipulation. We observe that `hdiff` has complex input data access patterns that can impact cache efficiency by incurring a significant number of cache misses, leading to sub-optimal performance on our current systems. The data that is used for `hdiff` is typically stored in a multi-dimensional array (referred to as a *grid*). `hdiff` computation requires access to input data elements in memory that are located both close to each other in memory (i.e., local memory access) and far apart in memory (i.e., global memory access). The local memory access patterns involve accessing the neighboring grid cells within the same row or column. Since

the input data is stored contiguously in memory, local access is relatively fast due to the spatial locality for which cache lines can be efficiently utilized. However, global memory access patterns require grid cells that are distant from the current cell in the input grid. Since the input data is not stored contiguously, global memory access is generally slower than local memory access. This type of access can lead to increased cache misses and latency. Therefore, it is crucial to optimize the memory access patterns to improve the performance of the `hdiff` computation.

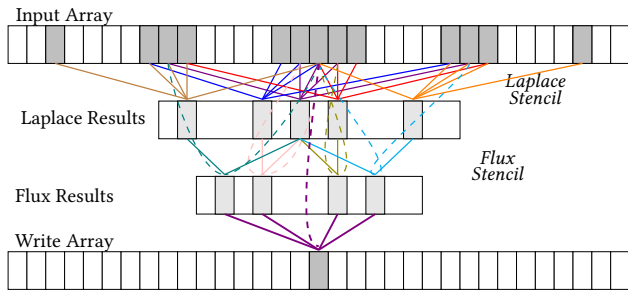


Figure 3: Memory layout of horizontal diffusion from 3D input grid onto 1D memory array. Each color represents a different stencil pattern that is a part of the `hdiff` computation. The dashed arrows represent the dependency of flux stencil on the input data.

2.2 Spatial Computing Architectures

A spatial architecture (such as [34–37]) consists of two-dimensional interconnected processing units. In AMD-Xilinx Versal [34], such a unit is referred to as an AI Engine (AIE) core, as shown in Figure 4.

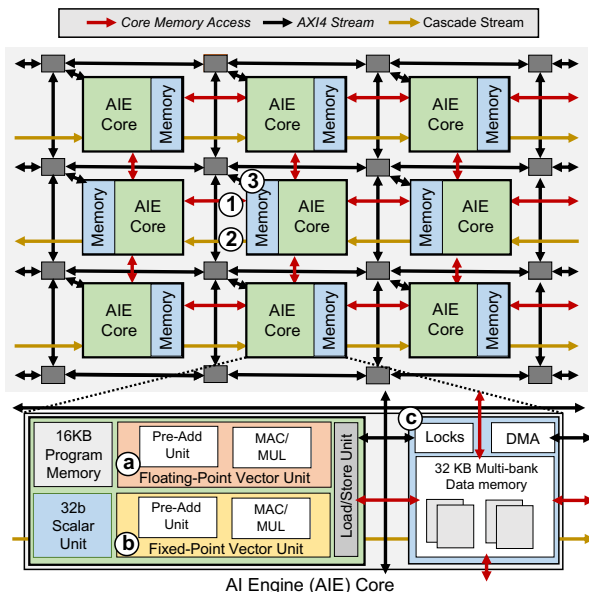


Figure 4: AI Engine (AIE) architecture overview. AIE consists of an array of processing cores interconnected through a highly configurable network. Each AIE core has independent datapaths for fixed-point and floating-point instructions with 32KB of local data memory.

The Versal platform has 400 of such AIE cores arranged in a checkerboard fashion. Each AIE core contains its own local program memory (16KB) and local data memory (32KB) and can execute instructions independently of all other cores. The AIE core is a VLIW processor that can issue up to seven instructions per cycle divided over two datapaths: a scalar and a vector. Due to these two independent datapaths, an AIE core can perform complex pointer arithmetic using the scalar datapath while fully utilizing the vector datapath. Each AIE core is clocked at 1GHz and programmed through C/C++ code using AIE intrinsics [46]. The vector datapath implements two-dimensional SIMD operations for both floating-point $\text{\textcircled{a}}$ and fixed-point vector units $\text{\textcircled{b}}$. The fixed-point datapath supports precisions ranging from 8-bit to 32-bit operands, which corresponds to 128 multiply and accumulate operations (MACs) to 8 MACs per cycle. The floating-point and fixed-point datapaths provide a *pre-add* unit for doing vector elementary functions, such as determining the minimum or maximum of two vectors or comparing two vectors. The AIE local data memory module $\text{\textcircled{c}}$ is divided into eight memory banks and also consists of a direct memory access (DMA) interface and locks. Locks allow synchronization between AIE cores, an AIE core and DMA, and an external memory-mapped AXI4 device (outside of the AIE array).

An AIE core can communicate with other AIE cores using three different interfaces [47], as shown in Figure 4: $\text{\textcircled{1}}$ *Core memory access*: direct load/store access to the memories of immediate neighboring AIE cores via a 256-bit interface, $\text{\textcircled{2}}$ *Cascade stream*: enables the transfer of (full accumulator precision) partial sums to a direct neighbor via a 384-bit interface, and $\text{\textcircled{3}}$ *AXI4 stream*: enables DMA to non-immediate AIE cores via two AXI-4 streams (also called as stream switches) of 32-bit. The core memory access interface allows access to the memory of neighboring AIE cores, leading to a total of 128-KiB contiguous data memory space (i.e., its own memory, the memory of the AIE core on the north, the memory of the AIE core on the south, and the memory of the AIE core on the east or west depending on the row and the relative placement of AIE core and memory module). The AXI4 stream interface can be configured to duplicate data to different AIE cores to enable input data *broadcast*, which allows multiple AIE cores to share the same input data. AIE also consists of 16 dedicated *shimDMA* (shim Direct Memory Access) cores in the bottom row for interfacing with external dynamic random-access (DDR) memory. A *shimDMA* is a lightweight DMA engine that provides a simplified interface for data movement between system memory and hardware accelerators. AIE consists of two 256-bit channels per *shimDMA* for read and write operations, respectively.

3 IMPLEMENTATION

To design SPARTA, we analytically examine the computation and memory requirements of `hdiff` for AIE (Section 3.1). Based on our analytical modeling, we propose, design, and implement two different AIE-based architectures: (1) *single-AIE*: single AIE core that performs both Laplacian and flux calculations (Section 3.2.1), and (2) *multi-AIE*: multiple AIE cores that compute Laplacian and flux on separate AIE cores (Section 3.2.2).

3.1 Analytical Modeling

Analysis of Computation Requirements. We first calculate the computation cycles requirement for `hdiff`. `hdiff` has five Laplacian stencils followed by four flux stencils, as shown in Algorithm 1. In every iteration, `hdiff` requires access to data from five rows of the input grid. Each Laplacian stencil performs five MAC operations, which are applied throughout the input grid except for the border region leading to $5 \times (R - 4) \times (C - 4)$ MAC operations, where R and C represent the number of rows and columns of a grid, respectively. As these operations are applied throughout the vertical dimension for all five Laplacian stencils, the total number of MAC operations is $5 \times (R - 4) \times (C - 4) \times D \times 5$, where D represents the number of planes of the input grid.

Each flux stencil requires 2 MAC operations, 1 subtract operation, 1 compare operation, and 1 select operation. In total, for the four flux stencils, we require $2 \times (R - 4) \times (C - 4) \times 4$ MAC operations and $1 \times (R - 4) \times (C - 4) \times 4$ operations each for subtract, compare, and select operations. The subtract, compare, and select operations use only the pre-add units in the vector datapath and not the MAC units.

In this work, we use the `int32` and `float32` data format due to the high-precision requirements in weather modeling [1]. `int32` and `float32` formats are widely used for weather modeling, depending on the specific requirements [48–58], e.g., regional weather modeling, ensemble modeling, and short-term weather forecasting. The use of higher precision allows for: (1) more accurate modeling of the complex interactions between the various physical processes involved in weather, such as temperature, pressure, moisture, and wind, and (2) the simulation of a wide range of time scales, from small-scale processes like cloud formation to large-scale phenomena, such as global weather patterns. Therefore, we can have a more accurate representation of the dynamics of weather systems over time. As a single AIE core is capable of 8×32-bit multiply-and-accumulate (MAC) operations in one clock cycle, the minimum number of cycles required for a complete sweep of `hdiff` on the input grid can be calculated using:

$$\text{Laplacian}_{comp} = \frac{5 \times (R - 4) \times (C - 4) \times D \times 5}{8} \quad (5)$$

$$\text{flux}_{comp} = \frac{2 \times (R - 4) \times (C - 4) \times D \times 4}{8} \quad (6)$$

$$+ \frac{3 \times (1 \times (R - 4) \times (C - 4) \times D \times 4)}{8}$$

$$\text{hdiff}_{comp} = \text{Laplacian}_{comp} + \text{flux}_{comp} \quad (7)$$

Where R , C , and D represent the number of rows, columns, and planes, respectively, of the input grid. This calculation assumes that all the MAC operations can be performed in parallel with 100% MAC efficiency.

Analysis of Memory Requirements. Next, we analyze the memory intensity (memory cycles) of `hdiff`. The coefficients for Laplacian and flux stencils can be stored in the vector registers, which avoids the need to fetch the coefficients from an AIE core data memory or shimDMA for each MAC operation. However, the input grid data needs to be tiled and loaded into the local data memory from the external memory for the MAC operations. An AIE core supports two 256-bit loads per cycle using the core memory access

interface. Laplacian needs to access $5 \times (R - 4) \times (C - 4) \times D \times 5$ elements and flux needs $2 \times (R - 4) \times (C - 4) \times D \times 4$ elements for a complete `hdiff` calculations. For 32-bit precision, the minimum number of memory cycles required for a complete sweep of `hdiff` on the input grid can be calculated as:

$$\text{Laplacian}_{mem} = \frac{5 \times (R - 4) \times (C - 4) \times D \times 5 \times 32}{2 \times 256} \quad (8)$$

$$\text{flux}_{mem} = \frac{2 \times (R - 4) \times (C - 4) \times D \times 4 \times 32}{2 \times 256} \quad (9)$$

$$\text{hdiff}_{mem} = \text{Laplacian}_{mem} + \text{flux}_{mem} \quad (10)$$

Discussion. The above high-level modeling provides a first-order estimate of external memory traffic and computation requirements, enabling the identification of parallelization and data-reuse opportunities. We make the following two observations. First, the Laplacian stencils have a more balanced design than flux stencils because the computation-to-memory intensity ratio of the Laplacian stencils (as represented by Equation 5 and Equation 8, respectively) is more balanced compared to the computation-to-memory intensity ratio of the flux stencils (as represented by Equation 6 and Equation 9, respectively). The flux stencils have a higher compute-bound (as represented by Equation 6) than the memory bound (as represented by Equation 9). Second, the non-MAC operations (subtract, compare, and select) in the flux stencil lead to higher computation cycles due to the frequent movement of data between accumulator and vector registers.

Our analytical modeling of `hdiff` on AIE leads to the insight that achieving the maximum throughput requires splitting the `hdiff` computation over multiple AIE cores. By splitting the `hdiff` computation over multiple cores, we obtain two main benefits. First, the compute-bound can be distributed among multiple cores, allowing for the concurrent execution of multiple stencil calculations, which can increase the overall performance and throughput of the `hdiff` algorithm. Second, it allows for the use of more AIE cores in parallel per shimDMA to achieve higher throughput.

3.2 Mapping onto the AIE Cores

For both our designs (single-AIE and multi-AIE), we carefully hand-tune the `hdiff` code to overlap memory operations with arithmetic operations, to improve performance. In multi-AIE, we use the AIE data forwarding interfaces to forward the results from the first AIE core (used for Laplacian calculation) to another AIE core (used for flux calculation). This approach allows for the concurrent execution of multiple stencil calculations to increase the overall performance and throughput of the `hdiff` design.

3.2.1 Single-AIE Core Mapping. Figure 5 shows the mapping of two Laplacian stencils, lap_{CR} and lap_{CRm} from Algorithm 1 (out of the five Laplacian stencils and four flux stencils needed for a single `hdiff` computation) onto an AIE core. We use the same AIE core to perform the remaining Laplacian and flux computations.

The weather data, based on the atmospheric model resolution grid, is stored in the DRAM of host system ①. We parallelize the computation across input planes. The limited on-chip memory per AIE core makes buffering entire 3D planes infeasible. Therefore, we tile the plane into smaller blocks with a sliding window that can

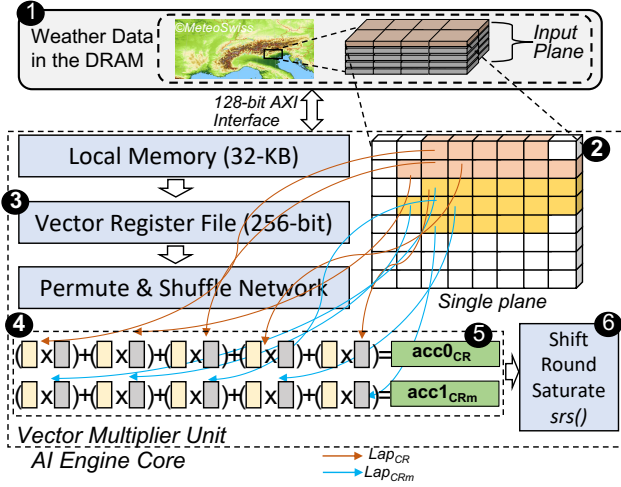


Figure 5: Mapping of two Laplacian stencils onto an AIE core datapath. We use the same AIE core to perform the Laplacian and flux computations. The weather data from the host DRAM is buffered into the local memory of an AIE core and further loaded into vector registers to perform hdiff computation.

fit into the on-chip memory. A single hdiff output computation requires access to data from five input rows of a single plane ②. Therefore, five rows are loaded into the local memory of an AIE core using a shimDMA core. We employ the double buffering (ping-pong) technique between the shimDMA and the core local memory to hide the transfer latency. From the local memory ③, the data is loaded into vector registers to perform the computations required for all the different Laplacian and flux stencils (see Section 2.1). We vectorize all the operations, e.g., lap_{CR} and lap_{CRm} perform five element-wise operations, each using the vector multiplier unit ④. We store partial results from each vector operation of a stencil in the same accumulator register ⑤. The programmer must ensure that there are not too many live registers (both vector and accumulator registers) as this can cause register spilling (i.e., the compiler would spill data onto the stack memory), resulting in wasted clock cycles. We allocate vector and accumulator registers among Laplacian and flux stencil computation making sure that there is no unnecessary spilling. It is essential to perform as many operations as possible while the data is in the accumulator register. We observe that the lap_{CR} calculation, as described in Algorithm 1, is utilized for all four subsequent flux stencil computations. Therefore, to minimize computation cycles and re-computation of results, we: (1) store the lap_{CR} accumulator results in a dedicated vector register using the shift-round-saturate intrinsic ($srs()$), and (2) reuse the lap_{CR} accumulator to perform as many flux stencil operations as possible.

For flux stencil, the non-MAC operations, such as vector addition/subtraction, vector compare, and vector selection, do not store data in an accumulator register as it uses the pre-adder unit that only has access to vector registers. Therefore, to continue with flux calculations after performing Laplacian operations, we need to send the data back from the accumulator registers to the vector registers using an $srs()$ operation (from shift round saturate unit ⑥ to vector register file ③). This operation has a long latency (4 cycles), which reduces the number of instructions that can be

completed within one cycle. Therefore, this process of moving data between registers can negatively impact performance and requires manual hand-tuning of the algorithm to hide data transfer latency. To overcome this, we carefully rearrange load/store, MAC/MUL, and non-MAC operations to fill the VLIW pipeline of the AIE core while avoiding NOPs. This rearrangement assists the compiler in proper scheduling and prevents multiple sequential load operations from filling the vector registers, which could lead to wasted VLIW instruction slots and decreased performance.

3.2.2 Multi-AIE Core Mapping. Based on our analytical modeling (Section 3.1), we create two multi-AIE designs: dual-AIE and tri-AIE. Figure 6 shows the multi-AIE design approach for hdiff, where the flux stencil uses the results of the Laplacian stencil to perform its computation. We also show the dataflow sequence from the external DRAM memory to the AIE cores. Instead of waiting for the Laplacian AIE core ③ to complete all five Laplacian stencils required for a single hdiff output, we forward the result of each Laplacian stencil to the flux AIE core ⑤, thereby allowing both cores to remain active. In tri-AIE design, we further split flux computation and map MAC operations and non-MAC operations onto different AIE cores.

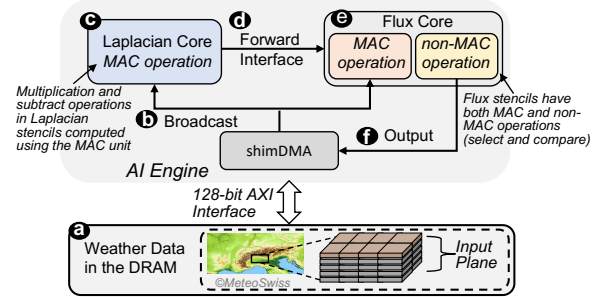


Figure 6: Multi-AIE design for hdiff computation to balance the computation and the memory bound. We show the dataflow sequence from the DRAM memory to the AIE cores via shimDMA.

As described in Algorithm 1, both Laplacian and flux computations require access to the input data, which is stored in the external DRAM ①. Therefore, we broadcast ② the input data onto the local memories of both Laplacian and Flux AIE cores using a single shimDMA channel. In dual-AIE design, a single Flux core is responsible for performing all MAC and non-MAC operations. As discussed in Section 3.1, flux operations have an imbalance between computation and memory bounds. Therefore, to further improve the compute performance, we split flux operations over two AIE cores in our tri-AIE design. We utilize the data forwarding interfaces to forward ④ the results of the Laplacian stencil computations from the first AIE core to the subsequent AIE core for flux stencil computation. After computing the output results, we transfer the results from the local memory of an AIE core to the external DDR memory ⑥.

3.3 Managing Data Transfer using MLIR

Versal provides a large number of AIE cores that can be interconnected using a wide range of interfaces. This complicates the effective management of dataflow between all the available cores.

We utilize MLIR (Multi-Level Intermediate Representation) [59] as a way to separate the AIE core computation optimization and code generation process in a flexible and modular manner. Our approach involves hand-optimizing code for an AIE core datapath and using MLIR to generate low-level code to connect the AIE cores and manage data transfer between the external DDR memory and AIE core memory.

We provide a code example for our single-AIE design in Code 1. We instantiate an AIE core and a shimDMA core (lines 2-3) to perform `hdiff` computation and transfer data from external memory to AIE core memory, respectively. We create two AIE object FIFOs for input and output data (lines 5-6). These FIFOs are circular queues [60] that buffer input data to exploit the data reuse in `hdiff`. We also create two external memory buffers to read (write) data to (from) the external DDR memory (lines 8-9). The AIE core inside a for-loop (line 15), acquires five elements from the input object FIFO for consumption (line 16) and one element from the output object FIFO for production (line 17) as `hdiff` requires five input grid rows to calculate a single output row. The `hdiff` computation is performed by calling a function `@vec_hdiff` (line 18) with the acquired subviews of input and output FIFOs (lines 16-17). In every loop iteration, we release one input row from the input FIFO to advance to the next row in the input grid (line 19) while producing an output row (line 20). After `hdiff` computation, all the remaining elements acquired from input FIFO are released (line 22), and the final results are transferred to the output DDR buffer using a shimDMA write channel.

```

1 module @hdiff_single_AIE{
2   %t71 = AIE.tile(7, 1) //AIE core at location 7,1
3   %t70 = AIE.tile(7, 0) //shimDMA at location 7,0
4   //setting input and output object FIFOs
5   %obj_in = AIE.objectFifo.createObjectFifo(%t70, {%t71}, 5)
6   {sym_name = "obj_in"} : !AIE.objectFifo<memref<i0xi32>>
7   %obj_out = AIE.objectFifo.createObjectFifo(%t71, {%t70},
8   {sym_name = "obj_out"} :
9   !AIE.objectFifo<memref<i0xi32>>
10  //allocating external DDR buffers
11  %ext_buffer_in = AIE.external_buffer {sym_name =
12  "ddr_test_buffer_in"} : memref<in1xi32>
13  %ext_buffer_out = AIE.external_buffer {sym_name =
14  "ddr_test_buffer_out"} : memref<out1xi32>
15  //point the object FIFOs to the external DDR buffers
16  AIE.objectFifo.registerExternalBuffers(%t70, %obj_in :
17  !AIE.objectFifo<memref<i0xi32>>, {%ext_buffer_in}) :
18  (memref<in1xi32>)
19  AIE.objectFifo.registerExternalBuffers(%t71, %obj_out :
20  !AIE.objectFifo<memref<i0xi32>>, {%ext_buffer_out}) :
21  (memref<out1xi32>)
22  //setting AIE core
23  %c13 = AIE.core(%t71) {
24  scf.for %iv = %lb to %ub step %step {
25  %obj_in_subview = AIE.objectFifo.acquire<Consume>(%obj_in
26  : !AIE.objectFifo<memref<i0xi32>>, 5) :
27  !AIE.objectFifoSubview<memref<i0xi32>>
28  %obj_out_subview =
29  AIE.objectFifo.acquire<Produce>(%obj_out :
30  !AIE.objectFifo<memref<i0xi32>>, 1) :
31  !AIE.objectFifoSubview<memref<i0xi32>>
32  func.call @vec_hdiff(%obj_in_subview,%obj_out_subview) : (
33  memref<i0xi32>, memref<i0xi32>) -> ()
34  AIE.objectFifo.release<Consume>(%obj_in :
35  !AIE.objectFifo<memref<i0xi32>>, 1)
36  AIE.objectFifo.release<Produce>(%obj_out :
37  !AIE.objectFifo<memref<i0xi32>>, 1)
38  }
39  AIE.objectFifo.release<Consume>(%obj_in :
40  !AIE.objectFifo<memref<i0xi32>>, 4)
41  AIE.end
42  } { link_with="hdiff.o" }
43 }

```

Code 1: MLIR code example for `hdiff` single-AIE design.

3.4 Scaling Accelerator Design

The performance of an implementation can be maximized by scaling it out across as many AIE cores as possible while avoiding an imbalance in processing resources caused by data starvation (i.e., ensuring that each core has access to the data it needs to complete its task). However, scaling a design on all the processing cores available on spatial computing systems is a non-trivial task. As discussed in Section 2.2, there are only 16 shimDMA cores for 400 AIE cores. System architects need to develop a design that can balance computation, memory, and communication resources. We observe four key challenges to scaling on spatial architectures: (1) balancing computation and memory resources, (2) limited shimDMA channels, (3) gathering and ordering of output results before sending them back to the external memory, and (4) placing input and output cores close to shimDMA to optimize data transfer. These challenges must be addressed in order to effectively scale the `hdiff` implementation across multiple AIE cores.

We address these challenges by developing an architecture that combines fewer off-chip data accesses with higher throughput for the loaded data. To this end, our accelerator design takes a data-centric approach [26, 61–76] that exploits dataflow spatial acceleration. We propose a *bundle* or *B-block*-based design. A B-block is a cluster of AIE cores connected to the same shimDMA input/output channel. As shown in Figure 7, clusters of AIE cores are connected to two channels of a shimDMA (one for input and one for output). Each B-block comprises of multiple *lanes* (or rows) of our tri-AIE design, with each lane calculating a different offset of output result using a part of the input plane. Based on our extensive empirical analysis to balance computation and memory performance, we choose four lanes for a B-block design.

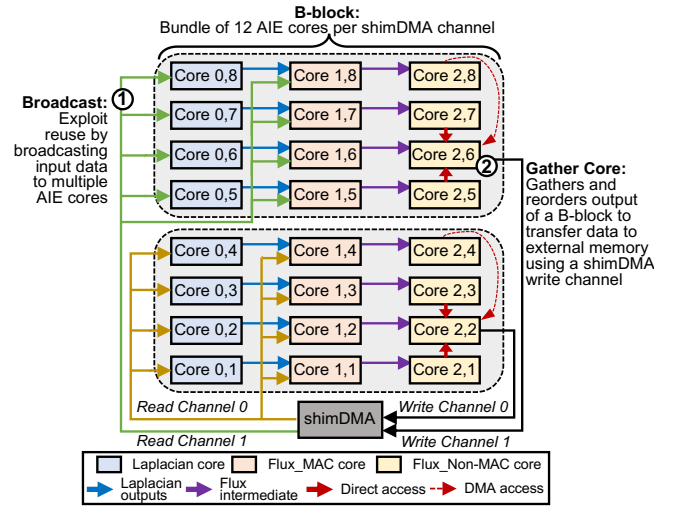


Figure 7: Block-based design (B-block) using tri-AIE implementation for `hdiff`. The B-block design allows scaling computation across the AIE cores while balancing computation and communication time without getting bottlenecked by limited shimDMA channels.

As each lane requires access to five rows of the input grid to perform a single `hdiff` computation, we use the broadcast feature

of the global interconnect to duplicate the eight rows of the input data into a circular buffer in the AIE cores of the first column ①. An 8-element circular buffer allows all the cores in the B-block lanes to work on a different offset of the input data while having five input grid rows necessary to perform `hdiff` computation.

Many spatial architectures lack support for automatically gathering and ordering computed outputs. To overcome this limitation, we use physical placement constraints to allow the AIE cores in the last column of a B-block to access a single shared memory of a dedicated AIE core, enabling data gathering. We refer to this core as the *gather core* ②. The gather core is responsible for collecting data from all other cores in a B-block, in addition to processing the results of its own lane. We use a core that lies in the middle of the B-block as the gather core and not a core located at either the top or bottom of the B-block due to the limited number of DMAs available on an AIE core. Each AIE core has only two DMAs. By placing the gather core in the middle of the B-block, we can directly access the memory of neighboring cores, reducing the total number of DMA operations required. If the gather core was placed at the top or bottom lane of a B-block, additional DMA operations would be needed to access the memories of further away cores, leading to higher data movement overhead and reducing overall performance. Therefore, placing the gather core in the middle of the B-block helps to reduce the data movement overhead by minimizing the distance between the gather core and the other cores in the block.

A single B-block operates on a single plane of the input data. Since two B-blocks can be connected to a single shimDMA, two planes can be served per shimDMA. This regular structure can then be repeated for all the 16 shimDMA cores present on the AIE device. Our B-block-based design is highly scalable and can be expanded to utilize 384 AIE cores (16 shimDMAs \times 2 B-blocks per shimDMA \times 12 AIE cores per B-block) while maintaining efficient resource allocation. Therefore, our B-block approach enables: (a) *modularity*: simplifies scaling as a B-block can be easily replicated and expanded to form a bigger system that can solve larger problem sizes, (b) *efficient resource utilization*: ensures that every AIE core and shimDMA is utilized effectively, which prevents resource starvation and maximizes system throughput, and (c) *load balancing*: ensures that all AIE cores in the B-block lanes are working on different offsets of the input data while having the necessary input grid rows to perform `hdiff` computation.

3.5 SPARTA Application Toolflow

Figure 8 shows the SPARTA application toolflow to support our architecture. We provide a B-block description to the SPARTA generator ①. The generator configures data movement across AIE cores, including appropriate input/output buffers and interconnect description. Our SPARTA generator is an elementary tool for generating stencil-based accelerators. It can be absorbed in the MLIR ecosystem as a *dialect* to create a custom, high-level intermediate representation (IR) that is tailored to the stencil application domain. Our hand-tuned SPARTA kernel code is compiled using the Vitis AIE Compiler [77] ② to generate object files (*.o). These object files are linked in our MLIR dataflow description (`aie.mlir`) and passed through MLIR-AIE [78] ③. MLIR-AIE is a custom IR tailored to AIE that generates low-level executable files (*.elf) for a target AMD Versal device. A software-defined host API ④ handles offloading

jobs to AIE cores with an interrupt-based queuing mechanism. This allows for minimal CPU usage (and, hence, power usage) during AIE operation.

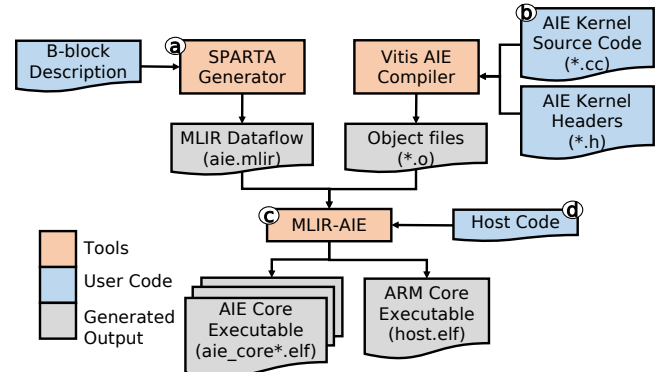


Figure 8: SPARTA application toolflow.

3.6 Elementary Stencil Workloads

We implement five elementary stencil workloads (`jacobi-1d` [79], `jacobi-2d-3pt` [79], `Laplacian` [14], `jacobi-2d-9pt` [79], `seidel-2d` [79]) that are frequently used as benchmarks for studying stencil computations [80–82].

Unlike `hdiff`, these stencils apply a single stencil pattern throughout the input grid. Therefore, such stencils have a higher arithmetic intensity than `hdiff`. We illustrate the mapping of elementary stencils on the AIE in Figure 9 using an elementary 3-point 2D stencil, i.e., `jacobi-2d-3pt`. This stencil performs three MAC operations to calculate a single output result. Since the stencil accesses three grid cells in three rows, we tile and load these three rows to an AIE core local memory for computation. Unlike our `hdiff` implementation, we do not split the computation of a single elementary stencil into dual-AIE or tri-AIE designs because these elementary stencils perform only a few operations.

While scaling these elementary stencil designs, a dedicated shimDMA channel is assigned to a specific AIE core; therefore, we enable as many shimDMA channels as the number of AIE cores. This dedicated connection allows us to use the shimDMA bandwidth effectively because each AIE core fetches from an independent shimDMA channel.

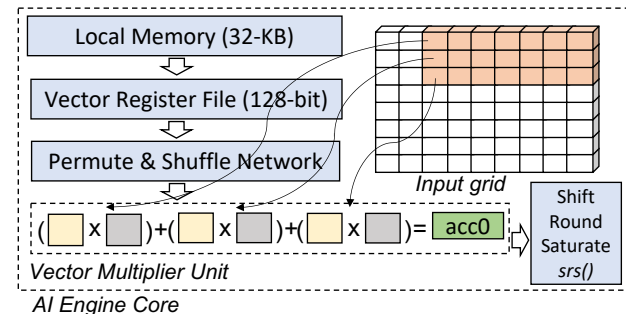


Figure 9: Mapping 3-point 2D Jacobi (`jacobi-2d-3pt`) elementary stencil onto an AIE core. Unlike `hdiff`, elementary stencils apply a single stencil pattern throughout the input grid.

4 EVALUATION

4.1 Experimental Methodology

We evaluate our accelerator designs for `hdiff` and five elementary stencils in terms of performance on an AMD-Xilinx Versal VCK190 [83] featuring Versal AI Core XCVC1902-2MSEVSVA2197 ACAP [84]. We use hardware locks to measure the end-to-end performance of AIE cores. Table 1 provides our system parameters and hardware configuration. We integrate our designs into the open-source MLIR-AIE framework [78]. We use 32-bit precision for all our implementations as used in production by the Swiss Federal Office of Meteorology and Climatology (MeteoSwiss) [85]. We generate highly optimized baseline code for CPU and GPU-based platforms using the official MeteoSwiss stencil benchmark suite [86]. We run all our experiments using a $256 \times 256 \times 64$ grid domain similar to the COSMO weather prediction model [13]. We open-source all our code at <https://github.com/CMU-SAFARI/SPARTA>.

Table 1: System parameters and hardware configuration for the baseline CPU, GPU, and AMD-Xilinx Versal.

CPU	AMD EPYC 7742 [87] @2.25GHz, 4-way SMT [88]
Cache-Hierarchy	32×32 KiB L1-I/D, 512 KiB L2, 256 MiB L3
System Memory	4×32GiB RDIMM DDR4 2666 MHz [89] PCIe 4.0 ×128
OS details	Ubuntu 21.04 Hirsute Hippo [90], GNU Compiler Collection (GCC) version 10.3.0 [91]
GPU	AMD Radeon Instinct™ MI50 [92] 3840 Stream Processors 32GB HBM2 PCIe 4.0 ×16, ROCm version 5.1.1 [93]
Versal	XCVC1902-2MSEVSVA2197 AI Core [84] 400×AI Engines @1GHz, 8GB DDR4 DIMM [94], Dual-Core Arm Cortex-A72 [95]

4.2 Performance Analysis Results

Single-AIE and Multi-AIE Designs. Figure 10 shows the execution time for `hdiff` on the AMD-Xilinx Versal platform using single-AIE and multi-AIE designs.

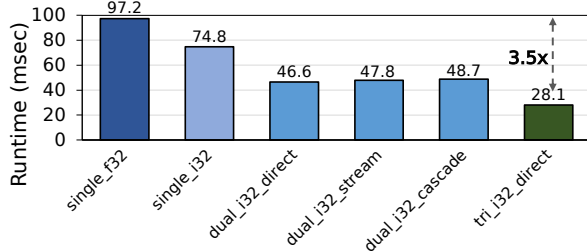


Figure 10: Runtime (ms) of `hdiff` using different designs.

We make the following three observations. First, the tri-AIE design (`tri_i32_direct`) improves performance by 3.5× compared to the single-AIE design with floating-point implementation (`single_f32`). This performance improvement is due to pipelining and balancing of Laplacian and flux computations using three separate cores, in addition to using the fixed-point datapath. Second, the multi-AIE designs (i.e., `dual_i32_direct`, `dual_i32_stream`, and `dual_i32_cascade`) improve performance by 1.94×–2.07× compared to the single-AIE design using fixed-point implementation, depending upon the data forwarding interface. The cascading interface provides the lowest improvements as it should only be used if the next AIE core would continue calculating while the data

is in the accumulator register. Otherwise, if the data needs to be returned to the vector register from the accumulator register, it would entail additional `srs()` latency of four clock cycles. Third, using a floating-point datapath (`single_f32`) instead of a fixed-point datapath (`single_i32`) leads to 1.3× higher execution time because: (1) there are no floating-point accumulator registers due to which we need to use vector registers for both vector operations and data accumulation, which leads to frequent register spilling, and (2) floating-point execution has longer latencies. We conclude that splitting computation across multiple AIE cores leads to a balance of computation, memory, and communication requirements, enabling higher performance.

Scaling Analysis. We provide the execution time of `hdiff` on the AMD-Xilinx Versal platform using the maximum possible AIE cores in Figure 11. We scale the number of B-blocks from 1 to the maximum number that we can accommodate using the available shimDMA channels. The maximum number of B-blocks is 32 while using 16 shimDMA cores that utilize 384 AIE cores (16 shimDMAs × 2 B-blocks per shimDMA × 12 AIE cores per B-block).

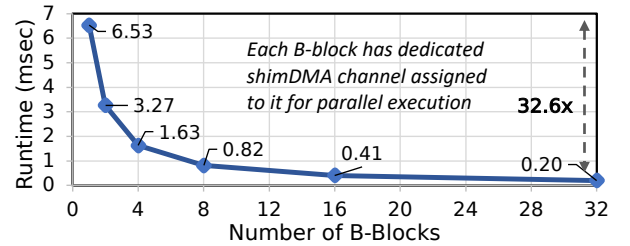


Figure 11: Runtime time (ms) of `hdiff` with different number of B-blocks.

Based on our analysis, we make three key observations. First, the full-blown SPARTA design (with the maximum number of B-blocks) provides 32.6× higher performance than a single B-block design. Second, a single B-block is 4.3× faster than our single tri-AIE design (`tri_i32_direct` in Figure 10). A single B-block processes different offsets of output data by broadcasting input data to all the lanes in the B-block while using the same shimDMA read/write channel. Broadcasting data to multiple AIE cores at once reduces the communication overhead associated with point-to-point data transfers. Third, the performance of `hdiff` scales linearly with the number of B-blocks, as all B-blocks have a dedicated shimDMA channel assigned to them. Having a dedicated shimDMA channel avoids contention in the memory channels. We conclude that our B-block design provides an efficient approach to scale `hdiff` implementation across multiple processing cores while having limited external memory interfaces in a spatial computing system.

4.3 Performance Comparison to the State-of-the-Art

Table 2 shows the performance comparison of SPARTA with state-of-the-art `hdiff` implementations. We mention their reported achieved performance (Perf. (GOp/s)) and calculate the percentage of achieved peak roofline performance (Arch. Roof. (%)) on their respective platforms. We make use of 384 AIE cores in SPARTA. We make the following two observations. First, SPARTA provides the highest performance with only 25.6 GB/s of external

memory bandwidth compared to all the other implementations, outperforming them by $1.2\times$ – $31.1\times$ in terms of GOP/s. Compared to the state-of-the-art CPU, GPU, and FPGA implementations of `hdiff`, SPARTA achieves $17.1\times$, $1.2\times$, and $2.1\times$ higher performance, respectively. Second, SPARTA achieves the highest peak roofline performance of 32.2%, while state-of-the-art implementations can reach only 1.6%–13.5% of the peak theoretical performance of a platform. This low peak performance is because weather stencils have several elementary stencils cascaded together with data dependencies that lead to complex and irregular memory access patterns. Using AIE-Power Estimator [96], we estimate the power of SPARTA as ~ 23.6 Watts (i.e., energy-efficiency of 42.19 GOPs/Watt). Compared to the state-of-the-art FPGA design [24] with 17.34 GOPs/Watt, SPARTA is $2.43\times$ more energy-efficient. We conclude that SPARTA provides both higher performance and higher energy efficiency compared to all state-of-the-art implementations on CPU, GPU, and FPGA-based computing systems.

4.4 Elementary Stencils Evaluation

Figure 12 shows the execution time comparison for elementary stencils on CPU, GPU, and AIE platforms.

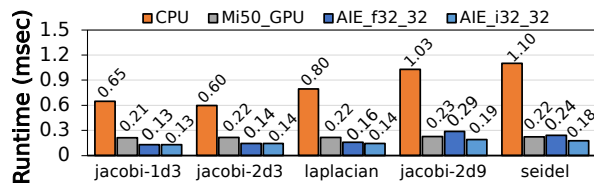


Figure 12: Runtime (ms) comparison for elementary stencils on AIE with CPU- and GPU-based platforms.

We scale computation to 32 AIE cores for elementary stencils as we develop a single AIE core design that can only access 32 shimDMA channels in parallel. We make the following two key observations. First, AIE-based design outperforms CPU-based implementation (CPU) by $4.5\times$ – $6.2\times$ and $1.5\times$ – $4.1\times$ for fixed-point (AIE_i32_32) and floating-point implementations (AIE_f32_32), respectively. Second, AIE, even with only 32 AI Engines, provides competitive performance compared to our baseline GPU system (Mi50_GPU) [92]. We conclude that the AIE platform provides efficient processing of stencil-based workloads by effectively balancing computation and data movement.

5 DISCUSSION

Spatial computing systems, with their high computation density through a large number of processing cores and customizability using a configurable interconnection network, offer significant promise to improve performance over modern multicore and heterogeneous systems. We present six key takeaways that we distill from our experimental design, analysis, and characterization on a state-of-the-art spatial computing system, i.e., the AMD-Xilinx Versal AI Engine architecture.

- **Key Takeaway #1. Workload balancing and parallelization across computation resources is important.** Spatial architectures provide a high degree of parallelism. To fully leverage this parallelism, it is essential to design the application such that computation is partitioned into parallelizable tasks. Our experimental

results utilizing a single AIE core-based design demonstrate that a lack of optimization in compute utilization can result in suboptimal resource utilization, leading to up to $2.77\times$ lower performance compared to a multi-AIE design using the same datapath.

- **Key Takeaway #2. Use broadcasting.** We exploit the broadcast feature of AIE that allows transferring data to multiple cores at the same time, which reduces data transfer overheads. SPARTA provides $4.3\times$ higher throughput per shimDMA channel by broadcasting data using our B-block-based approach.
- **Key Takeaway #3. Ease of programming is beneficial.** AIE-cores are software-programmable and can adapt to different applications without physical reconfiguration. Single-core AIE programming, similar to GPU programming, uses C/C++ constructs with intrinsics. However, the use of the MLIR framework for AIE programming allows developers to focus on high-level logic while handling lower-level details of code generation and optimization for different hardware targets. Such programming ease was helpful in our development and design space exploration.
- **Key Takeaway #4. Use the proper datatype with the highest computation density.** Using a fixed-point datapath can be more flexible and efficient for some applications. For example, SPARTA using the fixed-point datapath achieves $1.3\times$ higher performance compared to the floating-point datapath. The fixed-point datapath offers advantages such as: (1) support for dedicated accumulator registers, which allows for more efficient operations, (2) faster processing time, and (3) support for a wider range of precision options.
- **Key Takeaway #5. Use multiple accumulator/vector registers for parallel execution.** AIE provides 8×256 -bit vector and 4×384 -bit accumulator registers. We use multiple registers to: (1) allow dependence-free execution and (2) hide the latency of computation (e.g., since floating-point MAC has a latency of 2 cycles, we can schedule two MAC operations in a pipelined manner).
- **Key Takeaway #6. Assist compiler in better scheduling.** In order to assist the compiler in performing better scheduling, we restructure the code to reduce dependencies and improve parallelism. We achieve this by: (a) **interleaving memory and arithmetic operations:** by rearranging loads, MAC/MUL, and store operations, we maximize the use of the VLIW pipeline and avoid NOP instructions; (b) **avoiding register spilling:** we avoid having too many active registers (both vector and accumulators) since hardware can only support a limited number of registers (8×256 -bit vector and 4×384 -bit accumulator registers). Instantiating more variables than available registers leads to register spilling (i.e., causes data to spill onto stack memory, which reduces performance); (c) **shortening dependency length of a loop:** we load data for the first iteration outside of the loop body and for the next iteration at the end of a loop to shorten the dependency length of a loop.

6 RELATED WORK

To our knowledge, this is the first work to evaluate the benefits of using a cutting-edge spatial computing system for the horizontal diffusion stencils commonly used in real-world weather and climate modeling workloads [13, 15–20]. In this section, we describe various other related works on accelerating stencil processing.

Table 2: Overview and performance of the state-of-art hdiff implementations. For each work, we mention the DRAM memory technology (Mem. Tech.), theoretical peak floating-point performance (Peak Perf. (TFLOPS)), available peak memory bandwidth (Peak B/W (GB/s)), achieved performance (Perf. (GOp/s)), and the percentage of achieved peak roofline performance (Arch. Roof. (%)).

Stencil	Work	Year	Platform	Device	Mem. Tech.	Peak Perf. (TFLOPS)	Peak B/W (GB/s)	Perf. (GOp/s)	Arch. Roof. (%)
hdiff	[23]	2019	FPGA	XCVU3P [97]	DDR4	0.97	25.6	129.9	13.4%
hdiff	[16]	2021	CPU	Xeon E5-2690V3 [98]	DDR4	0.24	68.0	32.0	13.0%
hdiff	[24]	2021	CPU	POWER9 [31]	DDR4	0.49	110.0	58.5	11.8%
hdiff	[16]	2021	GPU	V100 [32]	HBM2	14.1	900.0	849.0	6.1%
hdiff	[16]	2021	FPGA	Stratix 10 [99]	DDR4	9.2	76.8	145.0	1.6%
hdiff	[24]	2021	FPGA	XCVU37P [97]	HBM	3.6	410.0	485.4	13.5%
hdiff	SPARTA	2023	AIE	XCVC1902 [83]	DDR4	3.1	25.6	995.7	32.2%

Stencil computation represents an important class of scientific workloads used in many high-performance computing applications, including computational fluid dynamics [100], image processing [101], weather prediction modeling [14], seismic imaging [102], electromagnetic simulations [103], heat diffusion [104], astrophysics [105], quantum computing [106], cellular automata [44], etc. Many past works focus on optimizing only elementary stencil computations [41, 42, 44, 80–82, 107–135]. However, *compound stencils*, which are made up of a series of elementary stencils that perform element-wise computations on a full 3D grid, are of great significance in real-world applications. Some past works use commodity devices that have a large market volume to accelerate compound stencil computations. For example, Bianco et al. [136] optimize the COSMO Model for GPU processing, while Thaler et al. [13] port COSMO to a many-core system. More recent works use FPGAs to accelerate compound stencils [16, 23, 24, 27]. However, taking full advantage of FPGAs to accelerate a workload is not trivial [137, 138]. Compared to CPUs or GPUs, an FPGA must exploit an order of magnitude more parallelism in a target workload to compensate for the lower clock frequency [23, 139–144]. We observe that real-world weather stencils have high hardware resource utilization and low peak performance because these stencils cannot easily leverage the bit-level flexibility available on FPGAs. Our work provides the first comprehensive evaluation of a state-of-the-art spatial architecture (that consists of an array of cores with a customizable interconnect) for real-world stencil computation.

7 CONCLUSION

Real-world climate and weather modeling applications require the use of complex compound stencil kernels that consist of a combination of different stencil computation patterns. Horizontal diffusion is a fundamental compound kernel, which is an important part of many climate and weather prediction models. State-of-the-art implementations of horizontal diffusion are memory bound with limited performance on current CPU, GPU, and FPGA-based computing systems. We propose SPARTA, a novel spatial accelerator for horizontal diffusion weather stencil computation. This work is the first to propose and evaluate a real spatial architecture (i.e., AMD-Xilinx Versal AI Engine) specifically for weather stencil computation, as opposed to commonly used machine learning-based workloads. Our results on a real spatial computing system demonstrate that SPARTA outperforms all state-of-the-art CPU, GPU, and FPGA implementations. We conclude that modern spatial architectures have the potential to provide both specialization and ease of

programming, surpassing the limitations of traditional platforms for real-world weather and climate modeling. We open-source all our code at <https://github.com/CMU-SAFARI/SPARTA> to facilitate reproducibility and ease of use as well as enable future research. We hope this work provides an important step towards using spatial computing systems for complex weather and climate modeling workloads.

ACKNOWLEDGMENTS

We thank the anonymous reviewers of ICS 2023 for their feedback. We thank the SAFARI Research Group members for valuable feedback and the stimulating intellectual and scientific environment they provide. SAFARI Research Group acknowledges the generous gifts of their industrial partners. This research was partially supported by the Semiconductor Research Corporation.

REFERENCES

- [1] P. Bauer, P. D. Dueben, T. Hoefler, T. Quintino, T. C. Schulthess, and N. P. Wedi, "The Digital Revolution of Earth-System Science," in *Nat. Comput. Sci.* 2021.
- [2] Z. Hausfather, H. F. Drake, T. Abbott, and G. A. Schmidt, "Evaluating the Performance of Past Climate Model Projections," in *Geophys. Res. Lett.*, 2020.
- [3] J. Slingo, P. Bates, P. Bauer, S. Belcher, T. Palmer, G. Stephens, B. Stevens, T. Stocker, and G. Teutsch, "Ambitious Partnership Needed for Reliable Climate Prediction," in *Nat. Clim. Change*, 2022.
- [4] J. Sillmann, T. Thorarindottir, N. Keenlyside, N. Schaller, L. V. Alexander, G. Hegerl, S. I. Seneviratne, R. Vautard, X. Zhang, and F. W. Zwiers, "Understanding, Modeling and Predicting Weather and Climate Extremes: Challenges and Opportunities," in *Weather. Clim. Extremes*, 2017.
- [5] T. Necker, D. Hinger, P. J. Griewank, T. Miyoshi, and M. Weissmann, "Guidance on How to Improve Vertical Covariance Localization Based on a 1000-Member Ensemble," in *NPG*, 2023.
- [6] V. Balaji, F. Couvreur, J. Deshayes, J. Gautrais, F. Hourdin, and C. Rio, "Are General Circulation Models Obsolete?" in *PNAS*, 2022.
- [7] G. Hu and S. L. Dance, "Efficient Computation of Matrix-Vector Products With Full Observation Weighting Matrices in Data Assimilation," in *Q. J. R. Meteorol. Soc.*, 2021.
- [8] S. L. Dance, S. P. Ballard, R. N. Bannister, P. Clark, H. L. Cloke, T. Darlington, D. L. A. Flack, S. L. Gray, L. Hawkness-Smith, N. Husnoo, A. J. Illingworth, G. A. Kelly, H. W. Lean, D. Li, N. K. Nichols, J. C. Nicol, A. Oxley, R. S. Plant, N. M. Roberts, I. Roulstone, D. Simonin, R. J. Thompson, and J. A. Waller, "Improvements in Forecasting Intense Rainfall: Results From the FRANCO (Forecasting Rainfall Exploiting New Data Assimilation Techniques and Novel Observations of Convection) Project," in *Atmosphere*, 2019.
- [9] G. Hu, S. L. Dance, R. N. Bannister, H. G. Chipilski, O. Guillet, B. Macpherson, M. Weissmann, and N. Yussouf, "Progress, Challenges, and Future Steps in Data Assimilation for Convection-Permitting Numerical Weather Prediction: Report on the Virtual Meeting Held on 10 and 12 November 2021," in *ASL*, 2023.
- [10] P. D. Dueben and P. Bauer, "Challenges and Design Choices for Global Weather and Climate Models Based on Machine Learning," in *GMD*, 2018.
- [11] R. Pyle, N. Jovanovic, D. Subramanian, K. V. Palem, and A. B. Patel, "Domain-Driven Models Yield Better Predictions at Lower Cost than Reservoir Computers in Lorenz Systems," in *Philos. Trans. R. Soc. A*, 2021.

- [12] L. Bonaventura, "A Semi-Implicit Semi-Lagrangian Scheme Using the Height Coordinate for a Nonhydrostatic and Fully Elastic Model of Atmospheric Flows," in *JCP*, 2000.
- [13] F. Thaler, S. Moosbrugger, C. Osuna, M. Bianco, H. Vogt, A. Afanasyev, L. Mosemann, O. Fuhrer, T. C. Schulthess, and T. Hoefler, "Porting the COSMO Weather Model to Manycore CPUs," in *PASC*, 2019.
- [14] G. Doms and U. Schättler, "The Nonhydrostatic Limited-Area Model LM (Lokalmodel) of the DWD. Part I: Scientific Documentation," in *DWD, GB Forschung und Entwicklung*, 1999.
- [15] T. Gysi, T. Grosser, and T. Hoefler, "MODESTO: Data-centric Analytic Optimization of Complex Stencil Programs on Heterogeneous Architectures," in *SC*, 2015.
- [16] J. de Fine Licht, A. Kuster, T. De Matteis, T. Ben-Nun, D. Hofer, and T. Hoefler, "StencilFlow: Mapping Large Stencil Programs to Distributed Spatial Computing Systems," in *CGO*, 2021.
- [17] T. Palmer, C. Brankovic, F. Molteni, S. Tibaldi, L. Ferranti, A. Hollingsworth, U. Cubasch, and E. Klinker, "The European Centre for Medium-Range Weather Forecasts (ECMWF) Program on Extended-Range Prediction," in *Bull. Am. Meteorol. Soc.*, 1990.
- [18] T. McClung, "Global Forecast System: Technical Implementation Notice 16-11 Amended," in *Nation Weather Service*, 2016.
- [19] J. W. Hurrell, M. M. Holland, P. R. Gent, S. Ghan, J. E. Kay, P. J. Kushner, J.-F. Lamarque, W. G. Large, D. Lawrence, K. Lindsay, W. H. Lipscomb, M. C. Long, N. Mahowald, D. R. Marsh, R. B. Neale, P. Rasch, S. Vavrus, M. Verstein, D. Bader, W. D. Collins, J. J. Hack, J. Kiehl, and S. Marshall, "The Community Earth System Model: A Framework for Collaborative Research," in *Bull. Amer. Meteorol. Soc.*, 2013.
- [20] S. Watanabe, T. Hajima, K. Sudo, T. Nagashima, T. Takemura, H. Okajima, T. Nozawa, H. Kawase, M. Abe, T. Yokohata, T. Ise, H. Sato, E. Kato, K. Takata, S. Emori, and M. Kawamiya, "MIROC-ESM 2010: Model Description and Basic Results of CMIP5-20c3m Experiments," in *GMD*, 2011.
- [21] D. M. Daley and J. C. Garand, "Horizontal Diffusion, Vertical Diffusion, and Internal Pressure in State Environmental Policymaking, 1989-1998," in *Am. Politics Res.*, 2005.
- [22] W. C. Skamarock and J. B. Klemp, "A Time-Split Nonhydrostatic Atmospheric Model for Weather Research and Forecasting Applications," in *J. Comput. Phys.*, 2008.
- [23] G. Singh, D. Diamantopoulos, C. Hagleitner, S. Stuijk, and H. Corporaal, "NAR-MADA: Near-Memory Horizontal Diffusion Accelerator for Scalable Stencil Computations," in *FPL*, 2019.
- [24] G. Singh, D. Diamantopoulos, C. Hagleitner, J. Gomez-Luna, S. Stuijk, O. Mutlu, and H. Corporaal, "NERO: A Near High-Bandwidth Memory Stencil Accelerator for Weather Prediction Modeling," in *FPL*, 2020.
- [25] G. Singh, "Designing, Modeling, and Optimizing Data-Intensive Computing Systems," in *arXiv*, 2022.
- [26] G. Singh, D. Diamantopoulos, J. Gómez-Luna, C. Hagleitner, S. Stuijk, H. Corporaal, and O. Mutlu, "Accelerating Weather Prediction Using Near-Memory Reconfigurable Fabric," in *TRETS*, 2022.
- [27] G. Singh, D. Diamantopoulos, S. Stuijk, C. Hagleitner, and H. Corporaal, "Low Precision Processing for High Order Stencil Computations," in *Springer LNCS*, 2019.
- [28] G. Singh, M. Alser, D. S. Cali, D. Diamantopoulos, J. Gómez-Luna, H. Corporaal, and O. Mutlu, "FPGA-based Near-Memory Acceleration of Modern Data-Intensive Applications," in *IEEE Micro*, 2021.
- [29] G. Singh, "Designing, Modeling, and Optimizing Data-Intensive Computing Systems," Ph.D. Dissertation, Eindhoven University of Technology, 2021.
- [30] S. Williams, A. Waterman, and D. Patterson, "Roofline: An Insightful Visual Performance Model for Multicore architectures," in *CACM*, 2009.
- [31] S. K. Sadasivam, B. W. Thompto, R. Kalla, and W. J. Starke, "IBM POWER9 Processor Architecture," in *IEEE Micro*, 2017.
- [32] NVIDIA, "NVIDIA Tesla V100 GPU Architecture," <https://images.nvidia.com/content/volta-architecture/pdf/volta-architecture-whitepaper.pdf>, 2017.
- [33] "ADM-PCIE-9H7-High-Speed Communications Hub," <https://www.alpha-data.com/dep/products.php?product=adm-pcie-9h7>.
- [34] K. Visser, "Versal: The Xilinx Adaptive Compute Acceleration Platform (ACAP)," in *FPGA*, 2019.
- [35] D. Abts, J. Ross, J. Sparling, M. Wong-VanHaren, M. Baker, T. Hawkins, A. Bell, J. Thompson, T. Khasai, G. Kimmell, J. Hwang, R. Leslie-Hurd, M. Bye, E. Creswick, M. Boyd, M. Venigalla, E. Laforge, J. Purdy, P. Kamath, D. Maheshwari, M. Beidler, G. Rosseel, O. Ahmad, G. Gagarin, R. Czekalski, A. Rane, S. Parmar, J. Werner, J. Sproch, A. Macias, and B. Kurtz, "Think Fast: A Tensor Streaming Processor (TSP) for Accelerating Deep Learning Workloads," in *ISCA*, 2020.
- [36] T. P. Morgan, "Intel's Exascale Dataflow Engine Drops X86 and von Neumann," The Next Platform, 2018.
- [37] M. La and A. Chien, "Cerebras Systems: Journey to the Wafer-Scale Engine," in *University of Chicago, Tech. Rep.* 2020.
- [38] J. Zhuang, J. Lau, H. Ye, Z. Yang, Y. Du, J. Lo, K. Denolf, S. Neuendorffer, A. Jones, J. Hu, D. Chen, J. Cong, and P. Zhou, "CHARM: Composing Heterogeneous Accelerators for Matrix Multiply on Versal ACAP Architecture," in *FPGA*, 2023.
- [39] G. Singh, M. Alser, A. Khodamoradi, K. Denolf, C. Firtina, M. B. Cavlak, H. Corporaal, and O. Mutlu, "A Framework for Designing Efficient Deep Learning-Based Genomic Basecallers," in *bioRxiv*, 2022.
- [40] J. A. Fisher, "Very Long Instruction Word Architectures and the ELI-512," in *ISCA*, 1983.
- [41] H. M. Waidyasooriya and M. Hariyama, "Multi-FPGA Accelerator Architecture for Stencil Computation Exploiting Spatial and Temporal Scalability," in *IEEE Access*, 2019.
- [42] K. Sano, Y. Hatsuda, and S. Yamamoto, "Multi-FPGA Accelerator for Scalable Stencil Computation with Constant Memory Bandwidth," in *TPDS*, 2014.
- [43] H. M. Waidyasooriya, Y. Takei, S. Tatsumi, and M. Hariyama, "OpenCL-Based FPGA-Platform for Stencil Computation and Its Optimization Methodology," in *TPDS*, 2017.
- [44] Y. Chi, J. Cong, P. Wei, and P. Zhou, "SODA: Stencil with Optimized Dataflow Architecture," in *ICCAD*, 2018.
- [45] J. de Fine Licht, M. Blott, and T. Hoefler, "Designing Scalable FPGA Architectures Using High-Level Synthesis," in *PPoPP*, 2018.
- [46] AMD, "AI Engine (AIE) r2p18," https://www.xilinx.com/htmldocs/xilinx2021_1/aieengine_intrinsics/intrinsics/index.html
- [47] AMD-Xilinx, "Versal ACAP AI Engine Architecture Manual," <https://www.xilinx.com/support/documentation/architecture-manuals/am009-versal-ai-engine.pdf>
- [48] F. Vaña, P. Düben, S. Lang, T. Palmer, M. Leutbecher, D. Salmond, and G. Carver, "Single Precision in Weather Forecasting Models: An Evaluation with the IFS," in *Mon. Weather Rev.*, 2017.
- [49] T. Kimpson, E. A. Paxton, M. Chantry, and T. Palmer, "Climate Change Modelling At Reduced Floating-Point Precision With Stochastic Rounding," in *Q. J. R. Meteorol. Soc.*, 2023.
- [50] T. Palmer, "Stochastic Weather And Climate Models," in *Nature Reviews Physics*, 2019.
- [51] S. Hatfield, M. Chantry, P. Düben, and T. Palmer, "Accelerating High-Resolution Weather Models With Deep-Learning Hardware," in *PASC*, 2019.
- [52] M. Chantry, H. Christensen, P. Dueben, and T. Palmer, "Opportunities And Challenges For Machine Learning In Weather And Climate Modelling: Hard, Medium And Soft AI," in *Philos. Trans. R. Soc.*, 2021.
- [53] M. Chantry, S. Hatfield, P. Dueben, I. Polichtchouk, and T. Palmer, "Machine Learning Emulation Of Gravity Wave Drag In Numerical Weather Forecasting," in *JAMES*, 2021.
- [54] L. Saffin, S. Hatfield, P. Düben, and T. Palmer, "Reduced-Precision Parametrization: Lessons From An Intermediate-Complexity Atmospheric Model," in *Q. J. R. Meteorol. Soc.*, 2020.
- [55] J. Yuval, P. A. O'Gorman, and C. N. Hill, "Use Of Neural Networks For Stable, Accurate And Physically Consistent Parameterization of Subgrid Atmospheric Processes With Good Performance At Reduced Precision," in *Geophys. Res. Lett.*, 2021.
- [56] M. Klöwer, P. Düben, and T. Palmer, "Number Formats, Error Mitigation, And Scope for 16-bit Arithmetics In Weather And Climate Modeling Analyzed With A Shallow Water Model," in *JAMES*, 2020.
- [57] E. A. Paxton, M. Chantry, M. Klöwer, L. Saffin, and T. Palmer, "Climate Modeling in Low Precision: Effects of Both Deterministic And Stochastic Rounding," in *J. Clim.*, 2022.
- [58] J. Ackmann, P. D. Dueben, T. Palmer, and P. K. Smolarkiewicz, "Mixed-Precision for Linear Solvers in Global Geophysical Flows," in *JAMES*, 2022.
- [59] C. Lattner, M. Amini, U. Bondhugula, A. Cohen, A. Davis, J. Pienaar, R. Riddle, T. Shpeisman, N. Vasilache, and O. Zinenko, "MLIR: Scaling Compiler Infrastructure for Domain Specific Computation," in *CGO*, 2021.
- [60] K. Denolf, M. Bekooij, J. Cockx, D. Verkest, and H. Corporaal, "Exploiting the Expressiveness of Cyclo-Static Dataflow to Model Multimedia Implementations," in *EURASIP JASP*, 2007.
- [61] O. Mutlu, S. Ghose, J. Gómez-Luna, and R. Ausavarungnirun, "Processing Data Where It Makes Sense: Enabling In-Memory Computation," in *MicPro*, 2019.
- [62] O. Mutlu, S. Ghose, J. Gómez-Luna, and R. Ausavarungnirun, "A Modern Primer on Processing in Memory," in *Emerging Computing: From Devices to Systems-Looking Beyond Moore and Von Neumann*. Springer, 2021.
- [63] S. Ghose, A. Boroumand, J. S. Kim, J. Gómez-Luna, and O. Mutlu, "Processing-in-Memory: A Workload-Driven Perspective," in *IBM JRD*, 2019.
- [64] J. Ahn, S. Hong, S. Yoo, O. Mutlu, and K. Choi, "A Scalable Processing-in-Memory Accelerator for Parallel Graph Processing," in *ISCA*, 2015.
- [65] G. Singh, L. Chelini, S. Corda, A. J. Awan, S. Stuijk, R. Jordans, H. Corporaal, and A.-J. Boonstra, "Near-Memory Computing: Past, Present, and Future," in *MicPro*, 2019.
- [66] G. Singh, J. Gomez-Luna, G. Mariani, G. F. Oliveira, S. Corda, S. Stuijk, O. Mutlu, and H. Corporaal, "NAPEL: Near-Memory Computing Application Performance Prediction via Ensemble Learning," in *DAC*, 2019.
- [67] K. Hsieh, S. Khan, N. Vijaykumar, K. K. Chang, A. Boroumand, S. Ghose, and O. Mutlu, "Accelerating Pointer Chasing in 3D-Stacked Memory: Challenges,

- Mechanisms, Evaluation,” in *ICCD*, 2016.
- [68] K. Hsieh, E. Ebrahimi, G. Kim, N. Chatterjee, M. O’Connor, N. Vijaykumar, O. Mutlu, and S. W. Keckler, “Transparent Offloading and Mapping (TOM): Enabling Programmer-Transparent Near-Data Processing in GPU Systems,” in *ISCA*, 2016.
- [69] J. Ahn, S. Yoo, O. Mutlu, and K. Choi, “PIM-Enabled Instructions: A Low-Overhead, Locality-Aware Processing-in-Memory Architecture,” in *ISCA*, 2015.
- [70] A. Boroumand, S. Ghose, Y. Kim, R. Ausavarungnirun, E. Shiu, R. Thakur, D. Kim, A. Kuusela, A. Knies, P. Ranganathan, and O. Mutlu, “Google Workloads for Consumer Devices: Mitigating Data Movement Bottlenecks,” in *ASPLOS*, 2018.
- [71] G. Singh, L. Chelini, S. Corda, A. J. Awan, S. Stuijk, R. Jordans, H. Corporaal, and A.-J. Boonstra, “A Review of Near-Memory Computing Architectures: Opportunities and Challenges,” in *DSD*, 2018.
- [72] G. Singh, R. Nadig, J. Park, R. Bera, N. Hajinazar, D. Novo, J. Gómez-Luna, S. Stuijk, H. Corporaal, and O. Mutlu, “Sibyl: Adaptive and Extensible Data Placement in Hybrid Storage Systems Using Online Reinforcement Learning,” in *ISCA*, 2022.
- [73] K. Vadel, L. Chelini, A. BanaGozar, G. Singh, S. Corda, R. Jordans, and H. Corporaal, “TDO-CIM: Transparent Detection and Offloading for Computation In-Memory,” in *DATE*, 2020.
- [74] S. Corda, G. Singh, A. J. Awan, R. Jordans, and H. Corporaal, “Platform Independent Software Analysis for Near Memory Computing,” in *DSD*, 2019.
- [75] O. Mutlu, “Intelligent Architectures for Intelligent Computing Systems,” in *DATE*, 2021.
- [76] A. Boroumand, S. Ghose, B. Akin, R. Narayanaswami, G. F. Oliveira, X. Ma, E. Shiu, and O. Mutlu, “Google Neural Network Models for Edge Devices: Analyzing and Mitigating Machine Learning Inference Bottlenecks,” in *PACT*, 2021.
- [77] “Vitis Unified Software Platform Documentation: Embedded Software Development (UG1400), <https://docs.xilinx.com/r/en-US/ug1400-vitis-embedded/Getting-Started-with-Vitis>.”
- [78] “MLIR-based AIEngine toolchain, <https://github.com/Xilinx/mlir-ae>.”
- [79] L.-N. Pouchet, “Polybench: The Polyhedral Benchmark Suite,” in *URL: <http://www.cs.ucla.edu/pouchet/software/polybench>*, 2012.
- [80] K. Datta, M. Murphy, V. Volkov, S. Williams, J. Carter, L. Oliker, D. Patterson, J. Shalf, and K. Yelick, “Stencil Computation Optimization and Auto-tuning on State-of-the-Art Multicore Architectures,” in *SC*, 2008.
- [81] K. Datta, S. Williams, V. Volkov, J. Carter, L. Oliker, J. Shalf, and K. Yelick, “Auto-tuning the 27-point Stencil for Multicore,” in *iWAPT*, 2009.
- [82] K. Datta, S. Kamil, S. Williams, L. Oliker, J. Shalf, and K. Yelick, “Optimization and Performance Modeling of Stencil Computations on Modern Microprocessors,” in *SIAM review*, 2009.
- [83] AMD-Xilinx, “Versal AI Core Series VCK190 Evaluation Kit, <https://www.xilinx.com/products/boards-and-kits/vck190.html>.”
- [84] AMD-Xilinx, “Versal Architecture and Product Data Sheet: Overview, https://www.xilinx.com/support/documentation/data_sheets/ds950-versal-overview.pdf.”
- [85] C. Osuna, T. Wicky, F. Thuring, T. Hoefler, and O. Fuhrer, “Dawn: A High-Level Domain-Specific Language Compiler Toolchain for Weather and Climate Applications,” in *Supercomput. Front. Innov.*, 2020.
- [86] MeteoSwiss, “Stencil Benchmarks, https://github.com/MeteoSwiss-APN/stencil_benchmarks.”
- [87] AMD, “Introducing 3rd Gen AMD EPYC™ Processors, <https://www.amd.com/en/events/epyc>.”
- [88] D. M. Tullsen, S. J. Eggers, and H. M. Levy, “Simultaneous Multithreading: Maximizing On-Chip Parallelism,” in *ISCA*, 1995.
- [89] MICRON, “RDIMM, <https://www.micron.com/products/dram-modules/rdimm>.”
- [90] Ubuntu, “Ubuntu 20.04.3 LTS (Focal Fossa), <https://releases.ubuntu.com/20.04/>.”
- [91] GCC Project, “GCC, the GNU Compiler Collection, <https://gcc.gnu.org/>.”
- [92] AMD, “AMD Radeon Instinct™ MI50 Accelerator (32GB), <https://www.amd.com/system/files/documents/radeon-instinct-mi50-datasheet.pdf>.”
- [93] AMD, “ROCm, <https://github.com/RadeonOpenCompute/ROCm>.”
- [94] AMD-Xilinx, “Memory Interfaces Design Hub - UltraScale DDR3/DDR4 Memory, <https://www.xilinx.com/support/documentation-navigation/design-hubs/dh0061-ultrascale-memory-interface-ddr4-ddr3-hub.html>.”
- [95] ARM, “ARM Cortex-A72 MPCore Processor Technical Reference Manual r0p3, <https://developer.arm.com/documentation/100095/0003>.”
- [96] AMD-Xilinx, “Xilinx Power Estimator (XPE), <https://www.xilinx.com/products/technology/power/xpe.html>.”
- [97] AMD-Xilinx, “Virtex UltraScale+, <https://www.xilinx.com/products/silicon-devices/fpga/virtex-ultrascale-plus.html>.”
- [98] Intel, “Intel Xeon Processor E5-2690 v3, <https://www.intel.com/content/www/us/en/products/sku/81713/intel-xeon-processor-e52690-v3-30m-cache-2-60ghz/specifications.html>.”
- [99] Intel, “Intel Stratix 10 FPGA and SoC FPGA, <https://www.intel.com/content/www/us/en/products/details/fpga/stratix/10.html>.”
- [100] H. Huynh, Z. J. Wang, and P. E. Vincent, “High-Order Methods for Computational Fluid Dynamics: A Brief Review of Compact Differential Formulations on Unstructured Grids,” in *Computers & Fluids*, 2014.
- [101] T. Hermosilla, E. Bermejo, A. Balaguer, and L. A. Ruiz, “Non-Linear Fourth-Order Image Interpolation for Subpixel Edge Detection and Localization,” in *IMAVIS*, 2008.
- [102] G. A. McMechan, “Migration by Extrapolation of Time-Dependent Boundary Values,” in *Geophys. Prospect.*, 1983.
- [103] A. Taflove, “Review of the Formulation and Applications of the Finite-Difference Time-Domain Method for Numerical Modeling of Electromagnetic Wave Interactions With Arbitrary Structures,” in *Wave Motion*, 1988.
- [104] M. Frigo and V. Strumpen, “The Memory Behavior of Cache Oblivious Stencil Computations,” in *J. Supercomput.*, 2007.
- [105] D. S. Balsara, “Higher-Order Accurate Space-Time Schemes for Computational Astrophysics—Part I: Finite Volume Methods,” in *Living Rev. Comput. Astrophys.*, 2017.
- [106] K. Kormann and A. Nissen, “Error Control for Simulations of a Dissociative Quantum System,” in *ENUMATH*, 2009.
- [107] W. Augustin, V. Heuveline, and J.-P. Weiss, “Optimized Stencil Computation Using In-Place Calculation on Modern Multicore Systems,” in *Euro-Par*, 2009.
- [108] R. De La Cruz, M. Araya-Polo, and J. M. Cela, “Introducing the Semi-Stencil Algorithm,” in *PPAM*, 2009.
- [109] H. Dursun, K.-i. Nomura, W. Wang, M. Kunaseth, L. Peng, R. Seymour, R. K. Kalia, A. Nakano, and P. Vashishta, “In-Core Optimization of High-Order Stencil Computations,” in *PDPTA*, 2009.
- [110] H. Dursun, K.-i. Nomura, L. Peng, R. Seymour, W. Wang, R. K. Kalia, A. Nakano, and P. Vashishta, “A Multilevel Parallelization Framework for High-Order Stencil Computations,” in *Euro-Par*, 2009.
- [111] S. Kamil, P. Husbands, L. Oliker, J. Shalf, and K. Yelick, “Impact of Modern Memory Subsystems on Cache Optimizations for Stencil Computations,” in *MSP*, 2005.
- [112] S. Krishnamoorthy, M. Baskaran, U. Bondhugula, J. Ramanujam, A. Rountev, and P. Sadayappan, “Effective Automatic Parallelization of Stencil Computations,” in *PLDO*, 2007.
- [113] Z. Li and Y. Song, “Automatic Tiling of Iterative Stencil Loops,” in *TOPLAS*, 2004.
- [114] J. Meng and K. Skadron, “Performance Modeling and Automatic Ghost Zone Optimization for Iterative Stencil Loops on GPUs,” in *SC*, 2009.
- [115] P. Micikevicius, “3D Finite Difference Computation on GPUs Using CUDA,” in *GGPU*, 2009.
- [116] L. Gan, H. Fu, W. Luk, C. Yang, W. Xue, and G. Yang, “Solving Mesoscale Atmospheric Dynamics Using a Reconfigurable Dataflow Architecture,” in *IEEE Micro*, 2017.
- [117] J. van Lunteren, R. Luijten, D. Diamantopoulos, F. Auernhammer, C. Hagleitner, L. Chelini, S. Corda, and G. Singh, “Coherently Attached Programmable Near-Memory Acceleration Platform and its Application to Stencil Processing,” in *DATE*, 2019.
- [118] A. Denzler, G. F. Oliveira, N. Hajinazar, R. Bera, G. Singh, J. Gómez-Luna, and O. Mutlu, “Casper: Accelerating Stencil Computations Using Near-Cache Processing,” in *IEEE Access*, 2023.
- [119] J. Li, X. Wang, A. Tumeo, B. Williams, J. D. Leidel, and Y. Chen, “PIMS: A Lightweight Processing-in-Memory Accelerator for Stencil Computations,” in *ISMS*, 2019.
- [120] A. Nguyen, N. Satish, J. Chhugani, C. Kim, and P. Dubey, “3.5-D Blocking Optimization for Stencil Computations on Modern CPUs And GPUs,” in *SC*, 2010.
- [121] H. Stengel, J. Treibig, G. Hager, and G. Wellein, “Quantifying Performance Bottlenecks of Stencil Computations Using the Execution-Cache-Memory Model,” in *ICS*, 2015.
- [122] O. Fuhrer, T. Chadha, T. Hoefler, G. Kwasniewski, X. Lapillonne, D. Leutwyler, D. Lüthi, C. Osuna, C. Schär, T. C. Schultness, and H. Vogt, “Near-Global Climate Simulation at 1 Km Resolution: Establishing a Performance Baseline on 4888 GPUs with COSMO 5.0,” in *GMD*, 2018.
- [123] A. Armejach, H. Caminal, J. M. Cebrian, R. González-Alberquilla, C. Adeniyi-Jones, M. Valero, M. Casas, and M. Moretó, “Stencil Codes on a Vector Length Agnostic Architecture,” in *PACT*, 2018.
- [124] H. E. Yantir, A. M. Eltawil, and K. N. Salama, “Efficient Acceleration of Stencil Applications through In-Memory Computing,” in *Micromachines*, 2020.
- [125] R. Wester and J. Kuper, “Deriving Stencil Hardware Accelerators from a Single Higher-Order Function,” in *CPA*, 2014.
- [126] M. Christen, O. Schenk, and H. Burkhart, “Patus: A Code Generation and Autotuning Framework for Parallel Iterative Stencil Computations on Modern Microarchitectures,” in *IPDPS*, 2011.
- [127] C. Olshanowsky, M. M. Strout, S. Guzik, J. Loffeld, and J. Hittinger, “A Study on Balancing Parallelism, Data Locality, and Recomputation in Existing PDE Solvers,” in *SC*, 2014.
- [128] T. Brandvik and G. Pullan, “SBLOCK: A Framework for Efficient Stencil-Based PDE Solvers on Multi-Core Platforms,” in *ICCTI*, 2010.
- [129] E. H. Phillips and M. Fatica, “Implementing the Himeno Benchmark with CUDA on GPU Clusters,” in *IPDPS*, 2010.
- [130] L. Szustak, K. Rojek, and P. Gepner, “Using Intel Xeon Phi Coprocessor to Accelerate Computations in MPDATA Algorithm,” in *PPAM*, 2013.

- [131] S. Wang and Y. Liang, "A Comprehensive Framework for Synthesizing Stencil Algorithms on FPGAs Using OpenCL Model," in *DAC*, 2017.
- [132] A. Sohrabizadeh, C. H. Yu, M. Gao, and J. Cong, "AutoDSE: Enabling Software Programmers to Design Efficient FPGA Accelerators," in *TODAES*, 2022.
- [133] E. Reggiani, E. Del Sozzo, D. Conficconi, G. Natale, C. Moroni, and M. D. Santambrogio, "Enhancing the Scalability of Multi-FPGA Stencil Computations via Highly Optimized HDL Components," in *TRETS*, 2021.
- [134] M. Koraei, O. Fatemi, and M. Jahre, "DCMI: A Scalable Strategy for Accelerating Iterative Stencil Loops on FPGAs," in *TACO*, 2019.
- [135] X. Tian, Z. Ye, A. Lu, L. Guo, Y. Chi, and Z. Fang, "SASA: A Scalable and Automatic Stencil Acceleration Framework for Optimized Hybrid Spatial and Temporal Parallelism on HBM-based FPGAs," in *arXiv*, 2022.
- [136] M. Bianco, T. Diamanti, O. Fuhrer, T. Gysi, X. Lapillonne, C. Osuna, and T. Schulthess, "A GPU Capable Version of the COSMO Weather Model," in *ISC*, 2013.
- [137] G. Singh, D. Diamantopoulos, J. Gómez-Luna, S. Stuijk, H. Corporaal, and O. Mutlu, "LEAPER: Fast and Accurate FPGA-based System Performance Prediction via Transfer Learning," in *ICCD*, 2022.
- [138] G. Singh, D. Diamantopoulos, J. Gómez-Luna, S. Stuijk, O. Mutlu, and H. Corporaal, "Modeling FPGA-Based Systems via Few-Shot Learning," in *FPGA*, 2021.
- [139] D. Diamantopoulos, B. Ringlein, M. Purandare, G. Singh, and C. Hagleitner, "Agile Autotuning of a Transprecision Tensor Accelerator Overlay for TVM Compiler Stack," in *FPL*, 2020.
- [140] S.-W. Jun, M. Liu, S. Lee, J. Hicks, J. Ankcorn, M. King, S. Xu, and Arvind, "BlueDBM: An Appliance for Big Data Analytics," in *ISCA*, 2015.
- [141] D. S. Cali, K. Kanellopoulos, J. Lindegger, Z. Bingöl, G. S. Kalsi, Z. Zuo, C. Firtina, M. B. Cavlak, J. Kim, N. M. Ghiasi, G. Singh, J. Gómez-Luna, N. A. Alserr, M. Alser, S. Subramoney, C. Alkan, S. Ghose, and O. Mutlu, "SeGraM: A Universal Hardware Accelerator for Genomic Sequence-to-Graph and Sequence-to-Sequence Mapping," in *ISCA*, 2022.
- [142] M. Alser, J. Lindegger, C. Firtina, N. Almadhoun, H. Mao, G. Singh, J. Gomez-Luna, and O. Mutlu, "From Molecules to Genomic Variations: Accelerating Genome Analysis via Intelligent Algorithms and Architectures," in *CSBJ*, 2022.
- [143] J. Lee, H. Kim, S. Yoo, K. Choi, H. P. Hofstee, G.-J. Nam, M. R. Nutter, and D. Jasek, "ExtraV: Boosting Graph Processing Near Storage With a Coherent Accelerator," in *VLDB*, 2017.
- [144] J. Jiang, Z. Wang, X. Liu, J. Gómez-Luna, N. Guan, Q. Deng, W. Zhang, and O. Mutlu, "Boyi: A Systematic Framework for Automatically Deciding the Right Execution Model of OpenCL Applications on FPGAs," in *FPGA*, 2020.